

Plasma-induced energy band evolution for two-dimensional heterogeneous anti-ambipolar transistors

Cite as: J. Vac. Sci. Technol. B 41, 053202 (2023); doi: 10.1116/6.0002888

Submitted: 14 June 2023 · Accepted: 1 August 2023 ·

Published Online: 22 August 2023



Simran Shahi,¹  Asma Ahmed,¹  Ruizhe Yang,²  Anthony Cabanillas,¹ Anindita Chakravarty,¹ Maomao Liu,¹ Hemendra Nath Jaiswal,¹ Yu Fu,³ Yutong Guo,¹ Satyajeetsinh Shaileshsin Jadeja,¹ Hariharan Murugesan,¹ Anthony Butler,³ Chu Te Chen,³  Joel Muhigirwa,¹ Mohamed Enaitalla,¹ Jun Liu,^{2,a)}  Fei Yao,^{3,b)}  and Huamin Li^{1,c)} 

AFFILIATIONS

¹Department of Electrical Engineering, University at Buffalo, The State University of New York, Buffalo, New York 14260

²Department of Mechanical and Aerospace Engineering, University at Buffalo, The State University of New York, Buffalo, New York 14260

³Department of Materials Design and Innovation, University at Buffalo, The State University of New York, Buffalo, New York 14260

Note: This paper is part of the Special Topic Collection Celebrating the Early Career Professionals Contributing to the Advancement of Microelectronics and Nanotechnology.

^{a)}Electronic mail: jliu238@buffalo.edu

^{b)}Electronic mail: feiyao@buffalo.edu

^{c)}Author to whom correspondence should be addressed: huaminli@buffalo.edu

ABSTRACT

With the rise of two-dimensional (2D) materials and nanoelectronics, compatible processes based on existing Si technologies are highly demanded to enable new and superior device functions. In this study, we utilized an O₂ plasma treatment as a compatible and tunable method for anionic substitution doping in 2D WSe₂. With an introduced WO_x layer, moderate or even degenerate doping was realized to enhance hole transport in WSe₂. By combining with 2D MoS₂, an evolution of the 2D heterogeneous junction, in terms of the energy band structure and charge transport, was comprehensively investigated as a function of applied electric fields. The heterogeneous WSe₂/MoS₂ junction can function as an antiambipolar transistor and exhibit exceptional and well-balanced performance, including a superior peak-valley ratio of 2.4×10^5 and a high current density of 55 nA/μm. This work highlights the immense potential of 2D materials and their engineering to seamlessly integrate with existing semiconductor technology and enhance the efficiency of future nanoelectronics.

Published under an exclusive license by the AVS. <https://doi.org/10.1116/6.0002888>

I. INTRODUCTION

As three-dimensional (3D) Si-based complementary metal oxide semiconductor (CMOS) technologies approach the miniaturization limit of channel length, two-dimensional semiconductors such as transition metal dichalcogenides (TMDs, such as MoS₂ and WSe₂), metal monochalcogenides (MMC, such as InSe and GeSe), elemental semiconductors (such as silicene, germanene, and phosphorene), and metal oxides (MO, such as CuO and SnO) have been considered as promising channel materials for next-generation energy-efficient nanoelectronics.^{1–3} Owing to confined charge transport in sub-1-nm body thickness and naturally self-passivated

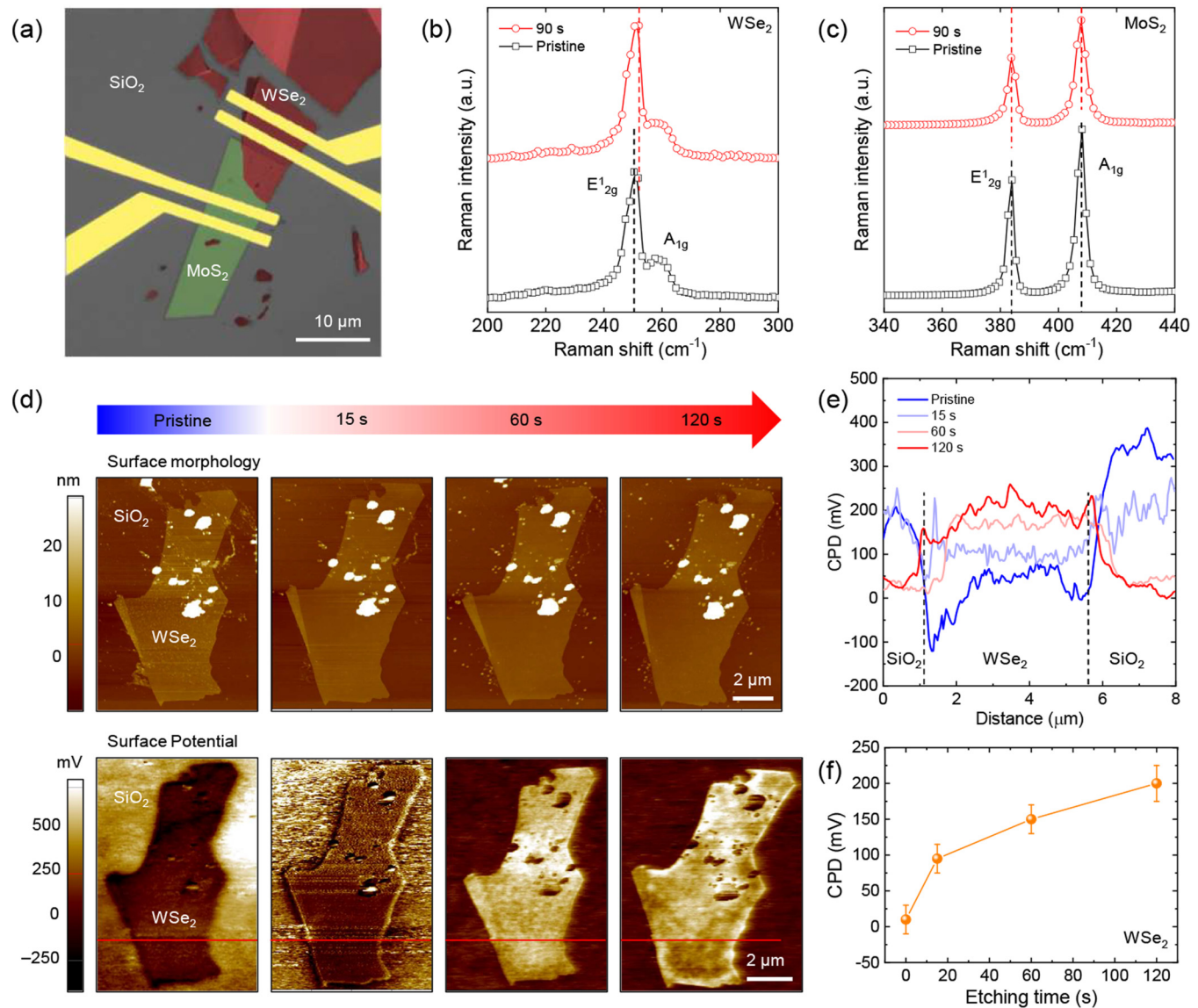
surface, these 2D layered materials are immune of a variety of scaling-induced unavoidable issues, including finite thickness variation, surface roughness and dangling bonds, and substantial degradation of charge transport in Si.^{4,5} Moreover, as more 2D materials being discovered, this layered material family possesses rich and diverse electronic properties that are comparable or superior to Si, such as lattice constant, bandgap, effective mass, carrier mobility, saturation velocity, and critical electric field.^{6–8} Owing to these advantages, novel field-effect transistor (FETs) concepts based on 2D semiconductors have been proposed and demonstrated. Taking the most representative 2D semiconductor MoS₂ as an example, these

24 August 2023 20:07:07

transistor prototypes include ultrashort channel FETs,^{9,10} tunnel FETs,^{11,12} ferroelectric FETs,¹³ negative capacitance FETs,¹⁴ Dirac source or cold source FETs,^{15–17} phase transition FETs,¹⁸ filament-based FETs,^{19–21} spin FETs,²² single electron FETs,²³ ambipolar FETs,²⁴ and antiambipolar FETs.²⁵

To realize specific functions of these 2D transistors and improve the device performance, plasma treatment stands as a reliable, compatible, and effective process.^{26,27} Composed of electrons,

ions, excited molecules, and radicals, plasma as the fourth state of matter can interact with 2D materials through different physical and chemical mechanisms and generate various modifications of material properties, including etching-induced thinning, electron or hole doping, phase transition, vacancy healing, and passivation. These interactions can be well controlled by a series of parameters, including plasma source, gas, pressure, frequency, power, and time. Especially with the ultrahigh surface-to-volume ratio of 2D

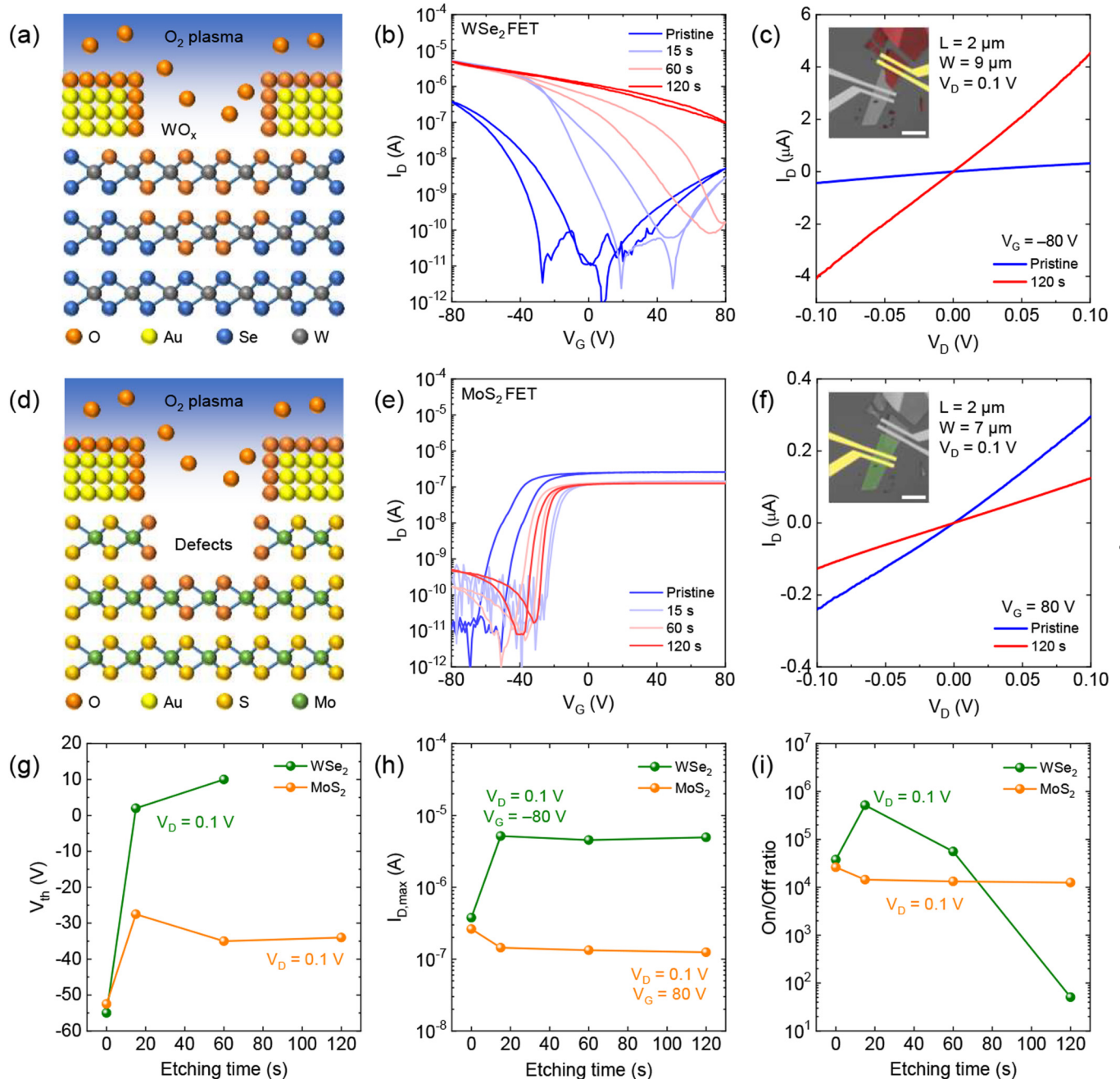


24 August 2023 20:07:07

FIG. 1. (a) False-color microscopy image of a WSe₂/MoS₂ FET on a SiO₂/Si substrate. (b) and (c) Comparison of Raman spectra of WSe₂ and MoS₂ before and after the O₂ plasma etching (90 s). (d) Surface morphology and potential mapping images of a WSe₂ flake on a SiO₂/Si substrate before and after the O₂ plasma etching (15, 60, and 120 s). (e) and (f) Variation of the CPD extracted from the mapping data in (d), indicated by a red line crossing both the WSe₂ and SiO₂ surface, and the averaged CPD of WSe₂ as a function of the etching time.

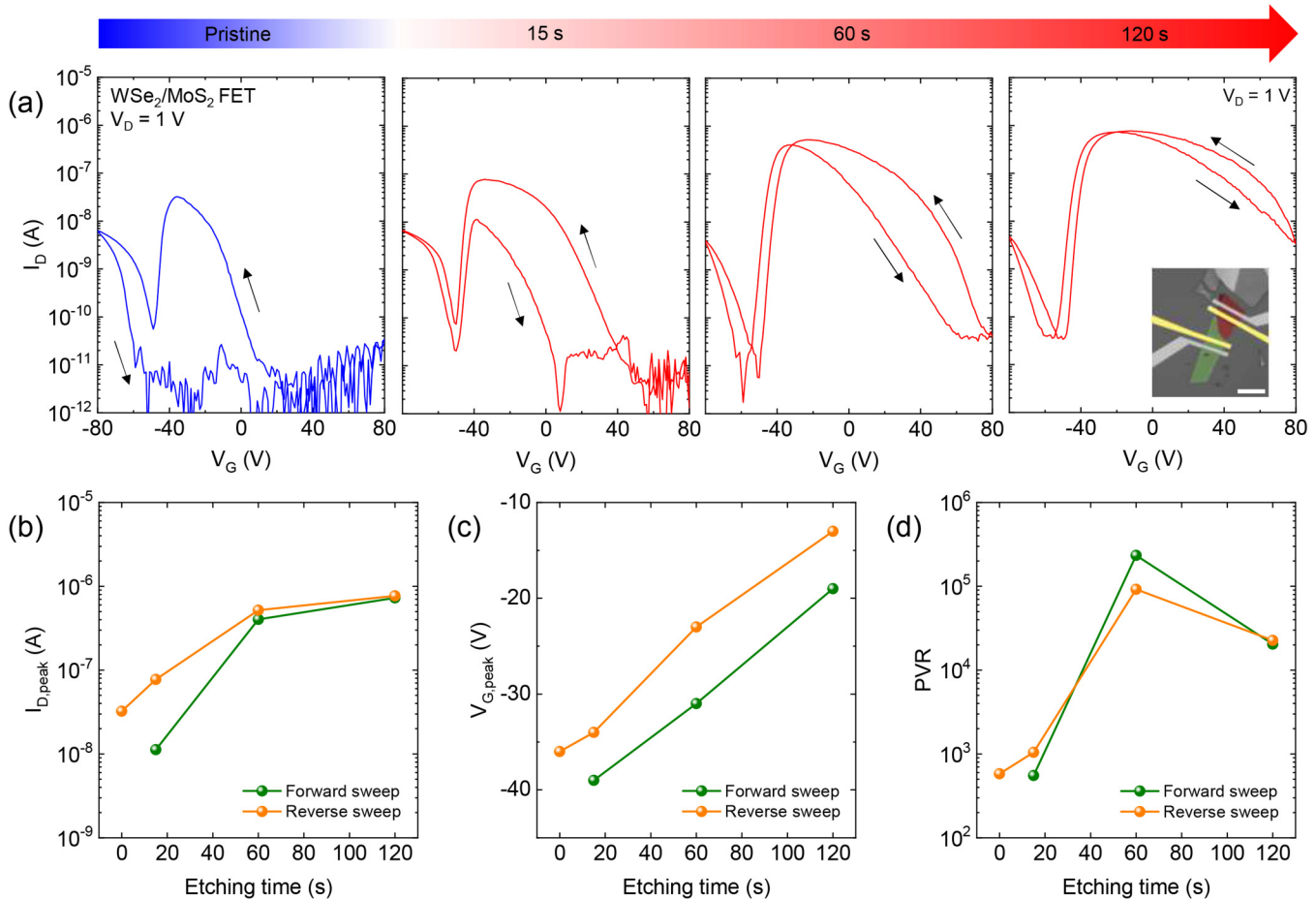
materials, the impact of the plasma treatment is more significant and effective compared to the case with 3D bulk materials. Taking the O_2 plasma treatment on 2D WSe_2 as an example, the process can form a surface oxide layer (WO_x , x approximates 3), introduce

a hole doping effect, and consequently provides a variety of benefits, such as atomic-scale etching,²⁸ suppressed contact resistance,^{29,30} improved transistor performance,^{31,32} highly sensitive photodetection,^{33,34} and formation of junction structures.^{34,35}



24 August 2023 20:07:07

FIG. 2. P-type doping effect of the O_2 plasma treatment on (a)–(c) WSe_2 and (d)–(f) MoS_2 FETs, including the schematics of the etching mechanism and an evolution of the transfer and output characteristics as the etching time increases. The inset of (c) and (f): microscopy images of the corresponding device configuration. Scale bar: $10 \mu m$. (g)–(i) Performance evolution of the WSe_2 and MoS_2 FETs as a function of the etching time, including V_{th} , $I_{D,max}$, and on/off ratio.



24 August 2023 20:07:07

FIG. 3. Performance evolution of the WSe₂/MoS₂ antiambipolar FET as a function of the etching time, including (a) transfer characteristics, (b) $I_{D,max}$, (c) on/off ratio, and (d) $V_{G,peak}$ in both forward and reverse sweeps. Inset of (a): microscopy image of the corresponding device configuration. Scale bar: 10 μ m.

Especially in the junction formation, both in-plane homogeneous junction and out-of-plane heterogeneous junction structures have been proposed for device applications.^{34,35} However, the evolution of energy band structure, interfacial states, and the corresponding carrier transport as a function of the O₂ plasma treatment has not been clearly revealed yet. With applied electric fields (perpendicular to or along the junction interface), these variations and their impacts on the device operation and performance become more complicated, constraining the design and implementation of the O₂ plasma treatment for the rise of 2D nanoelectronics.

In this work, we exploit the CMOS-compatible O₂ plasma treatment as an effective anionic substitution doping approach for 2D WSe₂ and demonstrate a heterogeneous WSe₂/MoS₂ junction as an antiambipolar FET with outstanding performance. Compared to conventional ambipolar FETs where the dominant charge carriers switch between electrons and holes with an applied gate voltage, the novel characteristic of the antiambipolar FETs is the convergence of both electron and hole branches to achieve a

peaked conductivity at an intermediate gate voltage.^{36,37} For 2D materials, the antiambipolar charge transport can be realized in 2D/2D or mixed-dimensional heterogeneous structures.^{25,38–42} Here, we exploited a novel plasma-induced oxidation and doping to achieve a controllable enhancement of hole transport in WSe₂ through moderate or even degenerate doping. By incorporating with 2D MoS₂ dominated by electron transport as well as the applied in-plane and out-of-plane electric fields, an evolution of the energy band structure of the 2D heterogeneous junction can be obtained, and the corresponding charge transport, dominated by the Fowler–Nordheim (FN) tunneling, is comprehensively elucidated. As an antiambipolar FET, our prototype device exhibits outstanding and balanced performance including a superior peak-valley ratio (PVR, 2.4×10^5) and a high current density (55 nA/ μ m). This work demonstrates the great potential of 2D materials and their doping engineering to feasibly integrate with the existing CMOS technology and eventually improve the efficiency of future nanoelectronics.

II. EXPERIMENT

A. Device fabrication and measurement

An optical microscope image of the anti-ambipolar FET based on a WSe₂/MoS₂ heterogeneous stacking structure is shown in Fig. 1(a). First, a MoS₂ flake is mechanically exfoliated from its bulk crystals, and then transferred on a Si wafer (0.001–0.005 Ω cm) which has a 285-nm thick SiO₂ layer. Next, a WSe₂ flake is exfoliated as well and transferred on top of the MoS₂ flake to form a partially overlapped heterostructure. A van der Waals (vdW) gap is expected at the heterogeneous interfaces, and it acts as electronically transparent due to the ultrathin spacing (about 0.3 nm). Then, multiple metal electrodes (Ti/Au, 1/100 nm) are patterned and deposited via electron beam lithography and evaporation (Elionix ELS-G100 and Kurt J. Lesker AXXIS). Taking one prototype device as an example, the thickness of MoS₂ and WSe₂ flakes is measured to be 45 and 25 nm, respectively, using an atomic force microscopy (AFM, Bruker Dimension Icon). The mapping of contact potential difference (CPD) is carried out using Kelvin probe force microscopy (KPFM) at room temperature to extract information such as surface potential and work functions. The channel length and width (*L* and *W*) of MoS₂, WSe₂, and WSe₂/MoS₂ FETs are 2 and 9 μm, 2 and 11 μm, as well as 11 and 9 μm, respectively. With a grounded source, drain current (*I_D*) is measured as a function of the applied drain voltage and gate voltage (*V_D* and *V_G*) and is normalized as drain current density (*I_D* = *I_D*/*W*) for benchmarking.

B. O₂ plasma doping

Anionic substitutional doping via the O₂ plasma treatment is applied on 2D materials and heterostructures using an inductively coupled plasma reactive ion etcher (ICP-RIE, Trion Tech Phantom III). The plasma treatment condition is optimized with 20 mTorr of the pressure, 11 W of the RIE power, and 98/20 SCCM of the O₂/Ar gas flow, leaving the exposure time as a solo variable parameter. For WSe₂, the O₂ plasma treatment bombards the surfaces with ions and creates anionic Se vacancies. Meanwhile, O free radicals occupy these vacancy sites and react with W to form WO_x. Due to a relatively higher work function (~6.5 eV compared to ~4.6 eV of WSe₂),^{43–45} WO_x acts as an effective p-type dopant and dope the underneath WSe₂ with holes.

C. Material characterization

Raman characterization (NanoBase XperRam, 532 nm of wavelength) is performed at room temperature, as shown in Figs. 1(b) and 1(c). Pristine multilayer WSe₂ exhibits an in-plane mode (*E_{2g}¹*) at around 250 cm⁻¹ and an out-of-plane mode (*A_{1g}*) at 258 cm⁻¹. After the O₂ plasma treatment for 90 s, a blue shift of the *E_{2g}¹* mode is obtained, suggesting a p-type doping effect.^{46,47} In contrast, pristine multilayer MoS₂ possesses *E_{2g}¹* and *A_{1g}* modes at 382 and 406 cm⁻¹, respectively. Both the modes remain consistent after the same plasma treatment, implying negligible impacts of the O₂ plasma treatment for MoS₂ in this work. Especially for WSe₂, the surface potential variation under O₂ plasma treatment is extracted as a function of the etching time, as shown in Figs. 1(d)–1(f). Being different from the reference SiO₂ surface which CPD declines

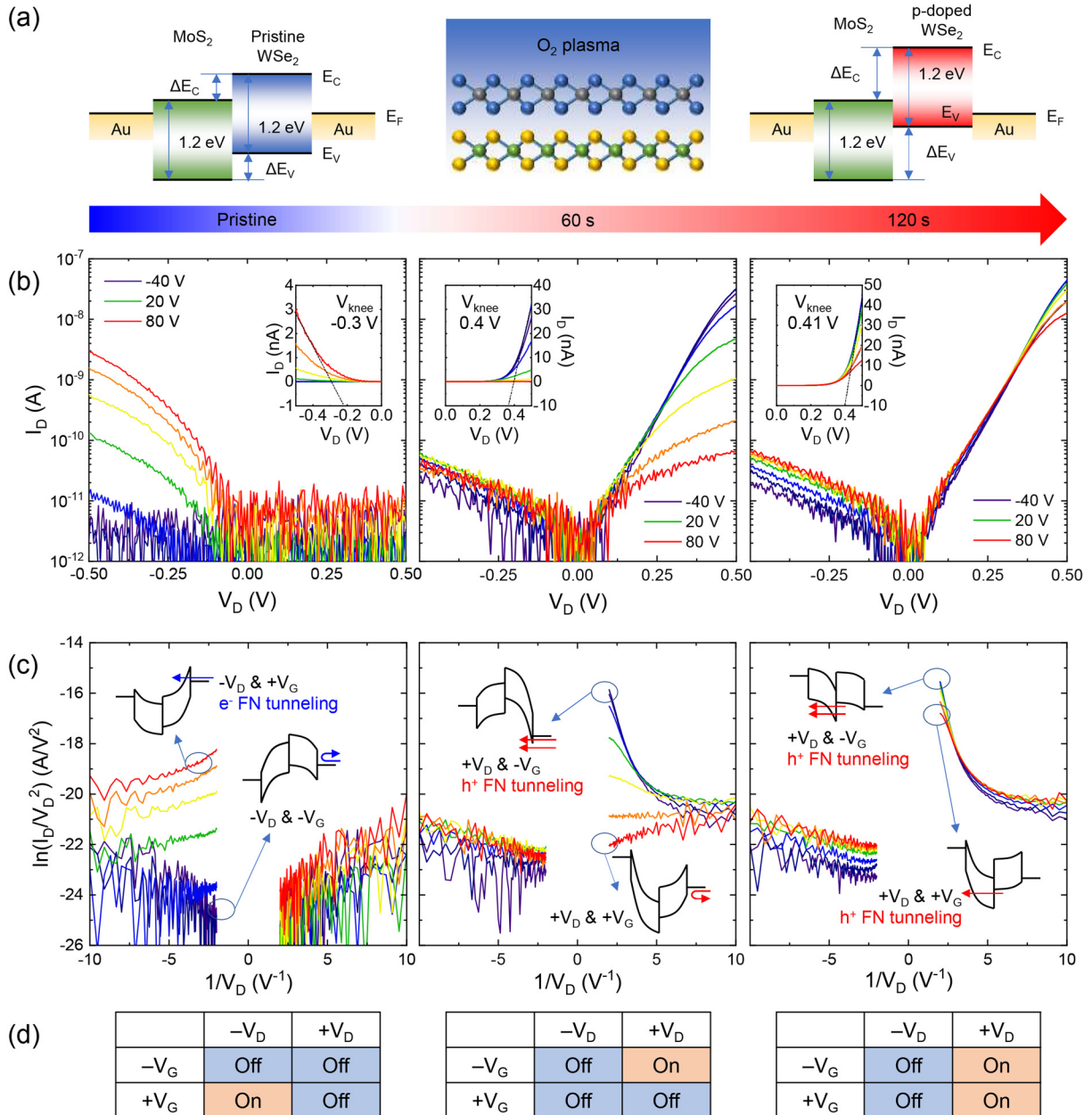
(from ~300 mV to about zero) as the plasma treatment continues, the CPD of WSe₂ increases substantially from ~10 to 200 mV, suggesting a significant change of the work function.⁴⁸ This result is also consistent with the doping effect as observed from the Raman spectroscopy analysis.

III. RESULTS AND DISCUSSION

The impact of the O₂ plasma etching on a WSe₂ FET is elucidated in Fig. 2(a). The O₂ plasma converts the exposed surface of WSe₂ to WO_x which extracts the electrons from the underneath WSe₂ layers and consequently generates a hole doping effect. According to *I_D*–*V_G* transfer characteristics, the pristine WSe₂ FET shows ambipolar charge transport, and the charge neutral point locates near zero *V_G*. As the O₂ plasma treatment is performed cumulatively from 15 to 60 and 120 s, the charge neutral point becomes increasingly positive until WSe₂ becomes degenerately doped with a suppressed gate modulation, as shown in Fig. 2(b). The hole current is promoted by about ten times at *V_G* = –80 V, and about 10⁵ at zero *V_G*, compared to the pristine case. *I_D*–*V_D* output characteristics possess a good linear current–voltage relationship before and after the plasma treatment, indicating an Ohmic contact condition at metal–semiconductor interfaces, as shown in Fig. 2(c). As a comparison, the response of a MoS₂ FET to the O₂ plasma etching is illustrated in Figs. 2(d)–2(f). The pristine MoS₂ FET shows typical electron-dominant unipolar charge transport starting at about *V_G* = –60 V. This is due to intrinsic doping and Fermi level pinning near the conduction band edge.⁴⁶ Instead of forming an oxide layer, the O₂ plasma treatment slightly damages the MoS₂ crystal structure and aggravates the formation of defects, dangling bonds, and vacancies. Although an Ohmic contact condition can still be maintained after the plasma treatment, the saturated electron current is decreased by about 50%. As a summary, the performance metrics of both WSe₂ and MoS₂ FETs, including the threshold voltage (*V_{th}*), the maximum *I_D* (*I_{D,max}*), and on/off ratio are presented as a function of the plasma treatment time, as shown in Figs. 2(g)–2(i). For the WSe₂ FET, *V_{th}* continues to evolve positively as the etching time increases, although *I_{D,max}* at *V_G* = –80 V reaches a saturation after 15 s of etching. The on/off ratio is degraded due to the degenerate doping which lowers the gating efficiency. In contrast, the MoS₂ FET is degraded and stabilized after 15 s of etching.

With the understanding of the individual WSe₂ and MoS₂ FETs, the evolution of the heterogeneous WSe₂/MoS₂ FET as a function of the plasma etching time is shown in Fig. 3. A clear anti-ambipolar charge transport peak is developed as the etching time increases, and the features including the maximum *I_D* and corresponding *V_G* of the antiambipolar peak (*I_{D,peak}* and *V_{G,peak}*) as well as the PVR value are summarized. For both forward and reverse sweeps, *I_{D,peak}* evolves to near 10⁻⁶ A after 120 s of etching, and *V_{G,peak}* shifts positively for about 20 V. The PVR is improved with the plasma treatment and reaches to the maximum up to 2.4 × 10⁵ after 60 s of etching. At this condition, the heterogeneous WSe₂/MoS₂ FET is optimized for antiambipolar charge transport since the less etching time (e.g., 15 s) causes a lower *I_{D,peak}* and the longer etching time (e.g., 120 s) leads to a doping-induced higher off current (or valley current).

24 August 2023 20:07:07



24 August 2023 20:07:07

FIG. 4. (a) Energy band structure of the WSe₂/MoS₂ junction at equilibrium before and after the plasma treatment. (b) and (c) Evolution of the output characteristics and FN tunneling characteristics as a function of the etching time. Here, V_G varies from -40 to 80 V with a step of 20 V. Inset of (b) reconstruction of the output characteristics in the linear scale for the V_{th} extraction. Inset of (c): corresponding energy band diagram at different V_D and V_G. (d) Summary of the diode behavior at different V_D and V_G as the plasma treatment progresses.

The antiambipolar charge transport is directly introduced by the unique energy band structure of the heterogeneous WSe₂/MoS₂ junction and its response to the applied electrostatic gating. Therefore, the I_D-V_D output characteristics of the WSe₂/MoS₂ FET

are carefully evaluated after each plasma treatment. The applied V_D provides an in-plane electric field to drive the charge injection and transport, whereas the applied V_G generates an out-of-plane electric field and capacitively modulates the doping level of 2D materials

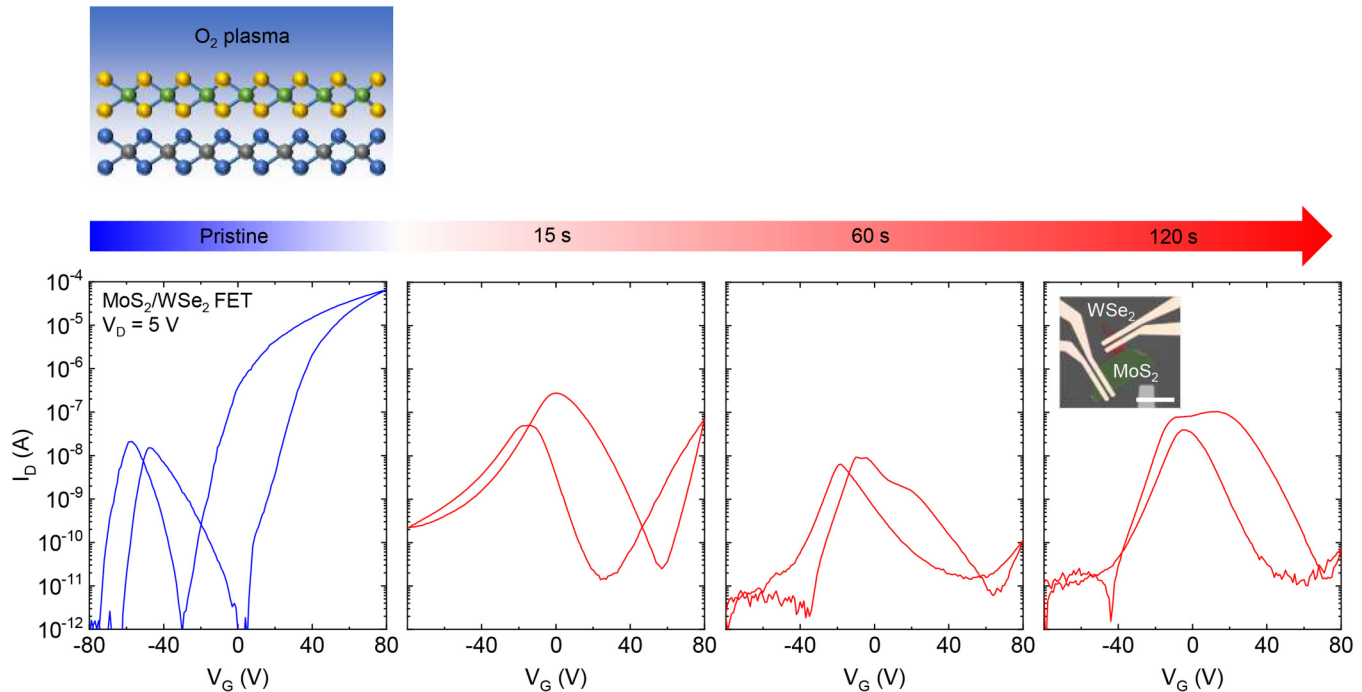


FIG. 5. Evolution of the transfer characteristics of a $\text{MoS}_2/\text{WSe}_2$ antiambipolar FET as a function of the etching time. Inset: microscopy image of the corresponding device configuration. Scale bar: $10\ \mu\text{m}$.

and, thus, the bending of energy band structures. First, the energy band structure of the $\text{WSe}_2/\text{MoS}_2$ junction before and after the O_2 plasma doping are compared, as shown in Fig. 4(a). Both MoS_2 and WSe_2 multilayers have the similar bandgaps of 1.2 eV. Owing to the WO_x -induced p-type doping, the work function of the WO_x/WSe_2 (Φ_{WSe_2}) layers becomes larger, compared to the unaffected work function of MoS_2 (Φ_{MoS_2}). As a result, a larger built-in potential energy barrier ($qV_{\text{bi}} = \Phi_{\text{WSe}_2} - \Phi_{\text{MoS}_2}$) at the $\text{WSe}_2/\text{MoS}_2$

interface is established as the etching time increases. Second, by assigning MoS_2 as grounded and applying a positive V_D at WSe_2 , the I_D - V_D output characteristics in the antiambipolar regime (-40 to $80\ \text{V}$) reveal a polarity transition after the plasma etching, as shown in Fig. 4(b). Meanwhile, the knee voltage (or cut-in voltage) shifts from -0.3 to $0.41\ \text{V}$ as $120\ \text{s}$ of the etching is applied, suggesting a drastic change of qV_{bi} , approximately $0.7\ \text{eV}$. Third, the data are reconstructed into $\ln(I_D/V_D^2)$ versus $1/V_D$ plots

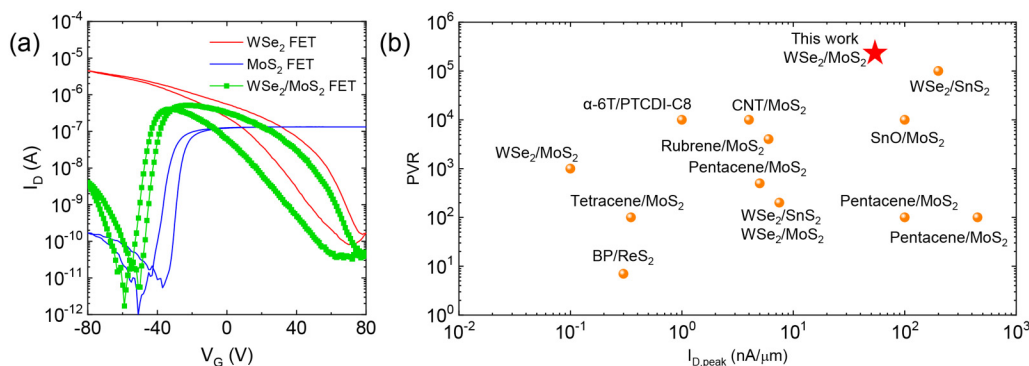


FIG. 6. (a) Antiambipolar transfer characteristics of the $\text{WSe}_2/\text{MoS}_2$ FETs bounded by the transfer curves of the individual WSe_2 and MoS_2 FETs. (b) Benchmarking of the PVR metric as a function of $I_{D,\text{peak}}$ for a variety of 2D antiambipolar FETs.

24 August 2023 20:07:07

to reveal the charge transport mechanism, as shown in Fig. 4(c). Linear decay from the high V_D (or zero $1/V_D$) center indicates the dominance of FN tunneling.^{49,50} In the pristine state, the charge transport in the V_G range of -40 to 80 V is mainly dominated by the electrons [see Figs. 2(b) and 2(e)], and their FN tunneling injection at the WSe_2 end is enabled when the negative V_D and positive V_G synergistically form a thin triangular electron barrier on the conduction band. After the plasma-induced p-type doping, the dominant charge is switched to the holes, and their FN tunneling injection through a thin triangular hole barrier on the valence band is enabled by the cooperation of the positive V_D and negative V_G . As V_G increases positively, the triangular barrier turns into a thicker and greater barrier and consequently diminishes the quantum tunneling probability and, thus, the current injection efficiency. When a degenerate p-type doping in WSe_2 is achieved after the plasma treatment, WSe_2 becomes less modulated by V_G , and an electronically transparent contact is established at the WSe_2 end. The valence band offset reaches to the maximum and approximates to qV_{bi} . The hole FN tunneling occurs at the WSe_2/MoS_2 interface at the positive V_D and shows a V_G dependence due to the varying thickness of the MoS_2 triangular barrier under the electrostatic gating. Finally, the on and off states of the WSe_2/MoS_2 junction at different V_D and V_G are summarized in Fig. 4(d). A clear evolution of the energy band structure and the corresponding charge transport is illustrated as a moderate-to-degenerate doping is applied on WSe_2 through a tunable O_2 plasma etching treatment.

In addition to the WSe_2/MoS_2 FET where WSe_2 is transferred on top of MoS_2 , we also fabricated the MoS_2/WSe_2 FET where the stacking order is reversed. It is anticipated that WSe_2 receives a stronger electrostatic gating in the MoS_2/WSe_2 FET, but only the exposed WSe_2 area can form WO_x by the O_2 plasma treatment and then develop a localized p-type doping effect. The experimental I_D-V_G transfer characteristics as a function of the plasma etching time are shown in Fig. 5. Similar to the WSe_2/MoS_2 FET, an evolution of the antiambipolar charge transport is obtained, suggesting the broad applicability of the O_2 plasma treatment for WSe_2 -based nanoelectronic devices, even with a variety of architectures.

Among the WSe_2/MoS_2 antiambipolar FETs prepared in this work, the best device exhibits an outstanding PVR value up to 2.4×10^5 at room temperature. The I_D-V_G transfer characteristics of the WSe_2/MoS_2 FET are presented in contrast with the individual WSe_2 and MoS_2 FETs after the identical plasma treatment, as shown in Fig. 6(a). It is clear that the antiambipolar charge transport behavior reflects the integration of the hole branch from WSe_2 and the electron branch from MoS_2 . The channel current is constrained by the counterpart material with a lower conductivity in a series connection and, consequently, presents a peak at the transition between the hole and electron dominance. We also benchmark the PVR and $I_{D,peak}$ metrics of our device with other heterogeneous antiambipolar FETs based on 2D materials including WSe_2 , MoS_2 , SnS_2 , and ReS_2 ,^{25,37,51–62} as shown in Fig. 6(b). Our device shows superior and balanced performance, and it can be further improved by architectural and processing optimization, for example, by adopting high- k dielectrics (e.g., HfO_2) to enhance the electrostatic gating and utilizing asymmetric contacts (e.g., Pt contacts for WSe_2 and Bi contacts for MoS_2) to promote the antiambipolar charge transport.

IV. SUMMARY AND CONCLUSIONS

In this work, we implement a CMOS-compatible O_2 plasma treatment to controllably introduce a p-type doping effect, ranging from moderate to even degenerate doping, on 2D semiconductor WSe_2 . As the plasma treatment progresses, the energy band evolution of a WSe_2/MoS_2 heterogeneous structure is evaluated, and the novel charge transport behavior under the applied electric fields is investigated for realizing an antiambipolar FET with outstanding and balanced performance.

ACKNOWLEDGMENTS

This work was mainly supported by the National Science Foundation (NSF) under Award No. ECCS-1944095 and partially supported by the New York State Center of Excellence in Materials Informatics (CMI). The authors acknowledge support from the Office of the Vice President for Research and Economic Development (OVPRED) at the University at Buffalo. A. Ahmed, A. Cabanillas, A. Chakravarty, J. Muhigirwa, and M. Enaitalla acknowledge support from the Arthur A. Schomburg Fellowship, the Presidential Fellowship, and the Collegiate Science and Technology Entry Program (CSTEP) at the University at Buffalo.

AUTHOR DECLARATIONS

Conflict of Interest

The authors have no conflicts to disclose.

Author Contributions

H. Li conceived the project and wrote the manuscript. F. Yao and J. Liu supervised the project. S. Shahi, A. Ahmed, A. Cabanillas, and Y. Guo performed the device fabrication and measurement. R. Yang, Y. Fu, A. Butler, and C. T. Chen performed the material characterization. A. Chakravarty, M. Liu, H. N. Jaiswal, S. Jadeja, and H. Murugesan assisted the data analysis and discussion. J. Muhigirwa and M. Enaitalla participated in the sample preparation.

Simran Shahi: Investigation (lead). **Asma Ahmed:** Investigation (equal). **Ruizhe Yang:** Investigation (equal). **Anthony Cabanillas:** Investigation (equal). **Anindita Chakravarty:** Investigation (equal). **Maomao Liu:** Investigation (equal). **Hemendra Nath Jaiswal:** Investigation (equal). **Yu Fu:** Investigation (equal). **Yutong Guo:** Investigation (equal). **Satyajeetsinh Shaileshsin Jadeja:** Investigation (equal). **Hariharan Murugesan:** Investigation (equal). **Anthony Butler:** Investigation (equal). **Chu Te Chen:** Investigation (equal). **Joel Muhigirwa:** Investigation (equal). **Mohamed Enaitalla:** Investigation (equal). **Jun Liu:** Supervision (equal). **Fei Yao:** Supervision (equal). **Huamin Li:** Conceptualization (lead); Writing – original draft (lead); Writing – review & editing (lead).

DATA AVAILABILITY

The data that support the findings of this study are available from the corresponding author upon reasonable request.

24 August 2023 20:07:07

REFERENCES

- ¹Y. Liu, X. Duan, H.-J. Shin, S. Park, Y. Huang, and X. Duan, *Nature* **591**, 43 (2021).
- ²M. Chhowalla, D. Jena, and H. Zhang, *Nat. Rev. Mater.* **1**, 16052 (2016).
- ³Y. Liu, X. Duan, Y. Huang, and X. Duan, *Chem. Soc. Rev.* **47**, 6388 (2018).
- ⁴Y. Shen *et al.*, *Adv. Mater.* **34**, 2201916 (2022).
- ⁵T. Wei, Z. Han, X. Zhong, Q. Xiao, T. Liu, and D. Xiang, *iScience* **25**, 105160 (2022).
- ⁶S. Das *et al.*, *Nat. Electron.* **4**, 786 (2021).
- ⁷K. Zhu, C. Wen, A. A. Aljarb, F. Xue, X. Xu, V. Tung, X. Zheng, H. N. Alshareef, and M. Lanza, *Nat. Electron.* **4**, 775 (2021).
- ⁸S. Wang, X. Liu, M. Xu, L. Liu, D. Yang, and P. Zhou, *Nat. Mater.* **21**, 1225 (2022).
- ⁹S. B. Desai *et al.*, *Science* **354**, 99 (2016).
- ¹⁰F. Wu, H. Tian, Y. Shen, Z. Hou, J. Ren, G. Gou, Y. Sun, Y. Yang, and T.-L. Ren, *Nature* **603**, 259 (2022).
- ¹¹D. Sarkar, X. Xie, W. Liu, W. Cao, J. Kang, Y. Gong, S. Kraemer, P. M. Ajayan, and K. Banerjee, *Nature* **526**, 91 (2015).
- ¹²X. Liu *et al.*, *ACS Nano* **11**, 9143 (2017).
- ¹³M. Si, P.-Y. Liao, G. Qiu, Y. Duan, and P. D. Ye, *ACS Nano* **12**, 6700 (2018).
- ¹⁴M. Si *et al.*, *Nat. Nanotechnol.* **13**, 24 (2018).
- ¹⁵M. Liu *et al.*, *ACS Nano* **15**, 5762 (2021).
- ¹⁶M. Liu, H. N. Jaiswal, S. Shahi, S. Wei, Y. Fu, C. Chang, A. Chakravarty, F. Yao, and H. Li, in *IEEE International Electron Devices Meeting (IEDM)*, San Francisco, CA, Virtual, 12–16 December (IEEE, Piscataway, NJ, 2020), pp. 12.5.1–12.5.4.
- ¹⁷Z. Tang, C. Liu, X. Huang, S. Zeng, L. Liu, J. Li, Y.-G. Jiang, D. W. Zhang, and P. Zhou, *Nano Lett.* **21**, 1758 (2021).
- ¹⁸B. Grisafe, N. Shukla, M. Jerry, and S. Datta, *IEEE International Symposium on VLSI Technology, Systems and Applications (VLSI-TSA)*, Hsinchu, Taiwan, 24–27 April (IEEE, Piscataway, NJ, 2017), p. 7942481.
- ¹⁹J. Lin *et al.*, *Adv. Sci.* **9**, 2104439 (2022).
- ²⁰Q. Hua *et al.*, *Nat. Commun.* **11**, 6207 (2020).
- ²¹S. G. Kim, S. H. Kim, G. S. Kim, H. Jeon, T. Kim, and H.-Y. Yu, *Adv. Sci.* **8**, 2100208 (2021).
- ²²W. Yan, O. Txoperena, R. Llopis, H. Dery, L. E. Hueso, and F. Casanova, *Nat. Commun.* **7**, 13372 (2016).
- ²³K. Lee, G. Kulkarni, and Z. Zhong, *Nanoscale* **8**, 7755 (2016).
- ²⁴W. Bao, X. Cai, D. Kim, K. Sridhara, and M. S. Fuhrer, *Appl. Phys. Lett.* **102**, 042104 (2013).
- ²⁵Y. Li, Y. Wang, L. Huang, X. Wang, X. Li, H.-X. Deng, Z. Wei, and J. Li, *ACS Appl. Mater. Interfaces* **8**, 15574 (2016).
- ²⁶J. Jadwiszczak, D. J. Kelly, J. Guo, Y. Zhou, and H. Zhang, *ACS Appl. Electron. Mater.* **3**, 1505 (2021).
- ²⁷H. Nan, R. Zhou, X. Gu, S. Xiao, and K. Ostrikov, *Nanoscale* **11**, 19202 (2019).
- ²⁸Z. Li, S. Yang, R. Dhall, E. Kosmowska, H. Shi, I. Chatzakakis, and S. B. Cronin, *ACS Nano* **10**, 6836 (2016).
- ²⁹I. Moon *et al.*, *Nanoscale* **11**, 17368 (2019).
- ³⁰C.-S. Pang, T. Y. T. Hung, A. Khosravi, R. Addou, Q. Wang, M. J. Kim, R. M. Wallace, and Z. Chen, *Adv. Electron. Mater.* **6**, 1901304 (2020).
- ³¹W.-M. Kang, S.-T. Lee, I.-T. Cho, T. H. Park, H. Shin, C. S. Hwang, C. Lee, B.-G. Park, and J.-H. Lee, *Solid State Electron.* **140**, 2 (2018).
- ³²K. Tang, X. Liu, Z. Wang, R. Wu, X. Dai, Y. Jing, J. Sun, and W. Luo, *Phys. Status Solidi RRL* **17**, 2200466 (2023).
- ³³S. B. Mitter, F. Ali, Z. Yang, I. Moon, F. Ahmed, T. J. Yoo, B. H. Lee, and W. J. Yoo, *ACS Appl. Mater. Interfaces* **12**, 23261 (2020).
- ³⁴H. Shin *et al.*, *Adv. Mater. Interfaces* **9**, 2201785 (2022).
- ³⁵X. Liu, Y. Pan, J. Yang, D. Qu, H.-M. Li, W. J. Yoo, and J. Sun, *Appl. Phys. Lett.* **118**, 233101 (2021).
- ³⁶Y. Ren, X. Yang, L. Zhou, J.-Y. Mao, S.-T. Han, and Y. Zhou, *Adv. Funct. Mater.* **29**, 1902105 (2019).
- ³⁷Y. Wakayama and R. Hayakawa, *Adv. Funct. Mater.* **30**, 1903724 (2020).
- ³⁸C. R. P. Inbaraj *et al.*, *ACS Nano* **15**, 8686 (2021).
- ³⁹W. Wang *et al.*, *ACS Nano* **16**, 11036 (2022).
- ⁴⁰R. Cheng *et al.*, *Adv. Mater.* **31**, 1901144 (2019).
- ⁴¹Y. Shingaya, A. Zulkefli, T. Iwasaki, R. Hayakawa, S. Nakaharai, K. Watanabe, T. Taniguchi, and Y. Wakayama, *Adv. Electron. Mater.* **9**, 2200704 (2023).
- ⁴²E. Wu, Y. Xie, Q. Liu, X. Hu, J. Liu, D. Zhang, and C. Zhou, *ACS Nano* **13**, 5430 (2019).
- ⁴³R. Kato, H. Uchiyama, T. Nishimura, K. Ueno, T. Taniguchi, K. Watanabe, E. Chen, and K. Nagashio, *ACS Appl. Mater. Interfaces* **15**, 26977 (2023).
- ⁴⁴D.-H. Kang, J. Shim, S. K. Jang, J. Jeon, M. H. Jeon, G. Y. Yeom, W.-S. Jung, Y. H. Jang, S. Lee, and J.-H. Park, *ACS Nano* **9**, 1099 (2015).
- ⁴⁵R. Zhang, D. Drysdale, V. Koutsos, and R. Cheung, *Adv. Funct. Mater.* **27**, 1702455 (2017).
- ⁴⁶C. Kim, I. Moon, D. Lee, M. S. Choi, F. Ahmed, S. Nam, Y. Cho, H.-J. Shin, S. Park, and W. J. Yoo, *ACS Nano* **11**, 1588 (2017).
- ⁴⁷C.-J. Park, H. J. Park, J. Y. Lee, J. Kim, C.-H. Lee, and J. Joo, *ACS Appl. Mater. Interfaces* **10**, 29848 (2018).
- ⁴⁸R. Yang, Z. He, S. Lin, W. Dou, Z. L. Wang, H. Wang, and J. Liu, *Nano Lett.* **22**, 9084 (2022).
- ⁴⁹L. Lemmo, A. Di Bartolomeo, F. Giubileo, G. Luongo, M. Passacantando, G. Niu, F. Hatami, O. Skibitzki, and T. Schroeder, *Nanotechnology* **28**, 495705 (2017).
- ⁵⁰A. Di Bartolomeo, F. Urban, M. Passacantando, N. McEvoy, L. Peters, L. Lemmo, G. Luongo, F. Romeo, and F. Giubileo, *Nanoscale* **11**, 1538 (2019).
- ⁵¹Y. Wang, W.-X. Zhou, L. Huang, C. Xia, L.-M. Tang, H.-X. Deng, Y. Li, K.-Q. Chen, J. Li, and Z. Wei, *2D Mater.* **4**, 025097 (2017).
- ⁵²A. Nourbakhsh, A. Zubair, M. S. Dresselhaus, and T. Palacios, *Nano Lett.* **16**, 1359 (2016).
- ⁵³D. Jariwala, S. L. Howell, K.-S. Chen, J. Kang, V. K. Sangwan, S. A. Filippone, R. Turrisi, T. J. Marks, L. J. Lauhon, and M. C. Hersam, *Nano Lett.* **16**, 497 (2016).
- ⁵⁴J.-K. Kim *et al.*, *Sci. Rep.* **6**, 36775 (2016).
- ⁵⁵J. Dong, F. Liu, F. Wang, J. Wang, M. Li, Y. Wen, L. Wang, G. Wang, J. He, and C. Jiang, *Nanoscale* **9**, 7519 (2017).
- ⁵⁶H. J. Park, C.-J. Park, J. Y. Kim, M. S. Kim, J. Kim, and J. Joo, *ACS Appl. Mater. Interfaces* **10**, 32556 (2018).
- ⁵⁷D. Jariwala, V. K. Sangwan, C.-C. Wu, P. L. Prabhumirashi, M. L. Geier, T. J. Marks, L. J. Lauhon, and M. C. Hersam, *Proc. Natl. Acad. Sci. U.S.A.* **110**, 18076 (2013).
- ⁵⁸Z. Wang, X. He, X.-X. Zhang, and H. N. Alshareef, *Adv. Mater.* **28**, 9133 (2016).
- ⁵⁹R. Yan *et al.*, *Nano Lett.* **15**, 5791 (2015).
- ⁶⁰J. Shim *et al.*, *Nat. Commun.* **7**, 13413 (2016).
- ⁶¹K. Kobashi, R. Hayakawa, T. Chikyow, and Y. Wakayama, *ACS Appl. Mater. Interfaces* **10**, 2762 (2018).
- ⁶²See the supplementary material online for more discussions regarding the Raman spectra and hysteresis characteristics in this work.



Jun Liu received his Ph.D. in Materials Engineering from the University of Alberta, Canada in 2018. He was a Postdoc Fellow in Chemical and Biological Engineering at SUNY Buffalo (2018–2020). He is currently an Assistant Professor in Mechanical and Aerospace Engineering, University at Buffalo. He is also an Associate Editor of *Energy Technology* (Wiley). His research is focused on understanding and manipulating fundamental physics at materials surface and interfaces for energy and sensing applications. He is the recipient of many awards such as 2022 SONY Faculty Innovation Award and 2020 Microsystem and Nanoengineering (MINE) Young Scientist Award (Springer Nature).

24 August 2023 20:07:07



Fei Yao received her dual Ph.D. degrees in Energy Science from Sungkyunkwan University, Korea and in Physics from Ecole Polytechnique, France, in 2013. She worked as postdoctoral researcher in the Center for Integrated Nanostructure Physics, Korea, and in the Department of Electrical Engineering, University of Notre Dame, USA. She is now an Assistant Professor in the Department of Materials Design and Innovation, University at Buffalo. Her research interests include low-dimensional materials synthesis and applications in energy storage and conversion.



Huamin Li has completed his Ph.D. from Sungkyunkwan University, Korea, and postdoctoral research from University of Notre Dame, USA. His expertise is in the exploration of two-dimensional materials and their application for high-performance energy-efficient nanoelectronics. He is currently serving as an Associate Editor Member in IEEE Access, Nano Express, and Materials Research Letters; a Technical Committee Member (Nanoelectronics) for Institute of Electrical and Electronics Engineers (IEEE) Nanotechnology Council; and an Executive Council Member for 2D Materials Technical Group in American Vacuum Society (AVS).